

Competing spin fluctuations in Sr_2RuO_4 and their tuning through epitaxial strain

Bongjae Kim ^{1,*}, Minjae Kim,² Chang-Jong Kang ³, Jae-Ho Han,⁴ and Kyoo Kim⁵


¹*Department of Physics, Kunsan National University, Gunsan 54150, Korea*

²*Korea Institute for Advanced Study, Seoul 02455, Korea*

³*Department of Physics, Chungnam National University, Daejeon 34134, Korea*

⁴*Center for Theoretical Physics of Complex Systems, Institute for Basic Science, Daejeon 34126, Korea*

⁵*Korea Atomic Energy Research Institute, 111 Daedeok-daero, Daejeon 34057, Korea*

 (Received 9 May 2022; revised 30 January 2023; accepted 23 March 2023; published 5 April 2023)

In this study, we report the magnetic energy landscape of Sr_2RuO_4 employing the generalized Bloch approach within density functional theory. We identify previously suggested magnetic fluctuations and ferromagnetic and spin-density-wave instabilities together with other predominant instabilities. We show that epitaxial strain can change the overall magnetic tendency of the system and tune the relative weight of the various magnetic instabilities in the system. Especially, the balance between spin-density-wave and ferromagnetic instabilities can be controlled by the strain and, eventually, can lead to new magnetic phases as well as superconducting phases with possibly altered pairing channels. Our findings are compared with previous theoretical models and experimental reports for the various magnetic features of the system and offers a first-principles explanation for them.

DOI: [10.1103/PhysRevB.107.144406](https://doi.org/10.1103/PhysRevB.107.144406)

I. INTRODUCTION

Since its first report, Sr_2RuO_4 has long been a system of interest due to its unconventional superconducting properties [1]. After intensive discussions on the superconductivity of the system, especially about the expectation of triplet pairing [2–6], a recent reexamination of the nuclear magnetic resonance experiments strongly suffocated the possibility of the chiral triplet pairing scenario [7]. This, however, renewed the interest in the system by permitting other order parameters and new candidates to float up from both theoretical and experimental studies [8–12].

Unlike other highly studied transition-metal-based superconductors, such as cuprates and Fe pnictides, Sr_2RuO_4 does not order magnetically and remains a paramagnetic metal in its normal state down to very low temperature. But the system is known to be very close to the magnetic phase, and a small perturbation, such as doping, easily makes the system magnetic [13–17]. The leading magnetic instabilities of the system are known to be ferromagnetic (FM) instabilities and spin-density-wave (SDW) instabilities with $\mathbf{q} \sim (0.3, 0.3, 0)\frac{2\pi}{a}$, denoted \mathbf{q}_{SDW} [18–21]. The former is from a Stoner instability, and the latter is known to be driven by interband nesting of the Fermi surfaces. The competition of the two magnetic instabilities is important because each one can lead to different types of pairing symmetry [22–26]. A recent polarized inelastic neutron scattering study revealed the dominance of the SDW contribution in the spin-fluctuation spectrum over the FM one [27], hence putting even more weight on the singlet scenario. But if we can control the

relative balance of the two competing magnetic instabilities, from the simple picture of spin fluctuation mediating pairing, we can expect the eventual tuning of the different types of the superconductivity pairing channels. Here, we pursue this direction through strain engineering.

In fact, the magnetism of Sr_2RuO_4 is not simple. In addition to the two well-known instabilities, FM and SDW, many magnetic responses with different \mathbf{q} have been noticed [20,28–31]. Of special note is the intraband-nesting instability at $\mathbf{q} \sim (1/2, 1/4, 0)\frac{2\pi}{a}$, which is expected to promote the odd-parity pairing in the uniaxially strained case [32]. From the density functional theory (DFT) approach, susceptibility calculations readily reproduced the reported SDW instabilities, and the combination of DFT with the many-body technique has offered further insights [23,33,34]. But the energetics, the strongest merit of the first-principles approach, of various magnetic phases of the system have not yet been presented from the DFT approaches. The magnetic energy scale of Sr_2RuO_4 is known to be well described by the DFT calculations despite the overestimating tendency towards magnetism [35]. That is, DFT, being a mean-field approach, gives a magnetically ordered ground state, while the system is paramagnetic. This is due to the inability of the DFT to depict the spin fluctuations, which destroy the static magnetic order in the real system. The DFT energetics of the system can still be employed wisely to generate magnetic exchange parameters that accurately reflect the system's magnetic susceptibility [35]. This means DFT unambiguously captures the instabilities on magnetic \mathbf{q} vectors. Hence, investigating the magnetic stability in larger ranges of the Brillouin zone would undoubtedly provide us with information on the involved magnetic fluctuations, leading to a better understanding of superconductivity in Sr_2RuO_4 .

*bongjae.kim@kunsan.ac.kr

In this paper, we investigate the magnetic energy landscape of Sr_2RuO_4 along the key \mathbf{k} paths with various \mathbf{q} values. We address the various magnetic fluctuations in the electronic structures of the system and look for the possibility of controlling the leading magnetic instabilities by employing epitaxial strain.

II. METHODOLOGY

A. DFT

All calculations were performed employing the Vienna Ab initio Simulation Package (VASP) [36,37]. The generalized gradient approximation (GGA) of Perdew, Burke, and Ernzerhof was utilized for the exchange-correlation functional [38]. An energy cut for the plane waves of 600 eV was used with a Monkhorst-Pack k mesh of $8 \times 8 \times 4$. We performed the full atomic relaxation for the nonstrained case (0% strain). For the epitaxial strain simulation, we fixed the in-plane lattice parameters based on the nonstrained one and fully relaxed the other degrees of freedom.

B. Generalized Bloch approach

Here, the spin spiral energetics calculations are performed employing the generalized Bloch approach. In the generalized Bloch theorem, we impose spin-spiral vector \mathbf{q} as a phase in addition to the Kohn-Sham wave function while keeping the Bloch condition. To describe the spiral vector of \mathbf{q} from the spin-polarized setup, we start with original spin-polarized Bloch functions of $\Phi_{\mathbf{k}}^{\sigma}(\mathbf{r})$, which is translationally invariant on the lattice vector \mathbf{R} . σ is spin index \uparrow or \downarrow . Then we can obtain a wave function of the spin-spiral system $\Psi_{\mathbf{k}}^{\sigma}(\mathbf{r})$ by imposing a phase factor from \mathbf{q} :

$$\begin{pmatrix} \Psi_{\mathbf{k}}^{\uparrow}(\mathbf{r}) \\ \Psi_{\mathbf{k}}^{\downarrow}(\mathbf{r}) \end{pmatrix} = \begin{pmatrix} e^{-i\mathbf{q}\cdot\mathbf{R}/2} & 0 \\ 0 & e^{+i\mathbf{q}\cdot\mathbf{R}/2} \end{pmatrix} \begin{pmatrix} \Phi_{\mathbf{k}}^{\uparrow}(\mathbf{r}) \\ \Phi_{\mathbf{k}}^{\downarrow}(\mathbf{r}) \end{pmatrix}.$$

Each up (\uparrow) and down (\downarrow) spinor gains an additional phase of $e^{-i\mathbf{q}\cdot\mathbf{R}/2}$ and $e^{+i\mathbf{q}\cdot\mathbf{R}/2}$, respectively. Hence, upon translation of one unit cell, the magnetic moment of an atom is rotated from the original unit cell by an angle of $\mathbf{q} \cdot \mathbf{R}$. Then the magnetization is expressed with the spin spiral \mathbf{q} . For example, for the spin-spiral \mathbf{q} vector along the z axis, the magnetization at $\mathbf{r} + \mathbf{R}$ is expressed as

$$m(\mathbf{r} + \mathbf{R}) = \begin{pmatrix} m_x(\mathbf{r}) \cos(\mathbf{q} \cdot \mathbf{R}) - m_y(\mathbf{r}) \sin(\mathbf{q} \cdot \mathbf{R}) \\ m_x(\mathbf{r}) \sin(\mathbf{q} \cdot \mathbf{R}) + m_y(\mathbf{r}) \cos(\mathbf{q} \cdot \mathbf{R}) \\ m_z(\mathbf{r}) \end{pmatrix}.$$

Here, the spin is effectively rotated within the x - y plane with the propagation vector along the z axis. This approach modulates the spin rotation, not the magnitude. That is, our approach describes the spiral SDW and differs from the longitudinal SDW. With this approach, we do not require the costly supercell calculations for the various \mathbf{q} , and also, frozen magnon spectra can be obtained. The details of the method are described in Refs. [39,40]. We employed the implementation in VASP [39,41]. For tetragonal Sr_2RuO_4 , we considered the k path which connects the high-symmetry points, Γ (0,0,0), X (0.5,0.5,0), and M (0.5,0,0), while changing k_x and k_y by 0.01.

TABLE I. Energy comparison of the explicit supercell calculation and spin-spiral calculation employing the generalized Bloch condition. For the supercell calculation, magnetic structures were explicitly imposed with $\mathbf{q} = (1/3, 1/3, 0)\frac{2\pi}{a}$, denoted $\mathbf{q}_{1/3}$. For the spin-spiral calculation, the closest \mathbf{q} value with $\mathbf{q} = (0.33, 0.33, 0)\frac{2\pi}{a}$, denoted $\mathbf{q}_{0.33}$, is compared. The values in parentheses are ones with the spin-orbit coupling calculations. $\mathbf{q}_{1/3}$ -udd and $\mathbf{q}_{1/3}$ -spiral denote the collinear and spiral configurations with the same $\mathbf{q}_{1/3}$ [35]. The unit of the energy difference is meV/Ru.

	Supercell			Spin spiral	
	FM	$\mathbf{q}_{1/3}$ -udd	$\mathbf{q}_{1/3}$ -spiral	FM	$\mathbf{q}_{0.33}$
Energy (meV)	0.0	-20.1 (-20.2)	-18.7 (-17.4)	0.0	-28.5

C. Validity check

To check the validity of our approaches, we first compared the energetics of the spin-spiral calculation with the result from the explicit supercell calculation. The anisotropic terms are much smaller than the isotropic ones, which was already identified with the previous calculations [35]. That is, longitudinal modulation can be approximated employing the spiral one with the same \mathbf{q} . Indeed, from the supercell calculations, the energy difference between collinear (up-down-down [udd]) and spiral-spin configurations with the same $\mathbf{q} = (1/3, 1/3, 0)\frac{2\pi}{a}$, denoted $\mathbf{q}_{1/3}$, is found to be 1.4 meV/Ru, which is much smaller than the energy difference between FM and $\mathbf{q}_{1/3}$ (around 20 meV/Ru; Table I). This shows that the long-range magnetic periodicity, as represented by the propagation vector \mathbf{q} , determines the overall magnetic energy landscape rather than the local anisotropic details of the magnetic exchanges and/or the modulation of the moment magnitudes. Then, we compared our spin-spiral calculation employing the generalized Bloch condition for approximate $\mathbf{q}_{1/3}$, $\mathbf{q} = (0.33, 0.33, 0)\frac{2\pi}{a}$, denoted $\mathbf{q}_{0.33}$. The result shows that although there is a small overestimation, the energy difference between the FM and $\mathbf{q}_{0.33}$ phases is on a scale (28.5 meV/Ru) similar to for the explicit supercell case. The overall magnetic energy scale does not change much with the inclusion of the spin-orbit coupling (Table I). With this, we can safely employ our spin-spiral calculation using the generalized Bloch condition without spin-orbit coupling for the description of magnetic energetics. As noted before, the spin-spiral calculation is very tricky and is sometimes unstable for different volume cases [41], and we have found that for a compressive strain of -3% and greater, the energetics description is not reliable and collapses to the nonmagnetic solution. This is expected from the previous calculation of monolayer ruthenates, in which for the unrotated RuO_6 octahedra case, the magnetism vanishes for a compressive strain of -3% or more [42].

III. RESULTS AND DISCUSSION

A. Energetics and instabilities

In Fig. 1, we plot the energetics of spin-spiral calculations with the wave vector \mathbf{q} along the symmetric two-dimensional path Γ - X - M - Γ for various biaxial strain cases. Let us first

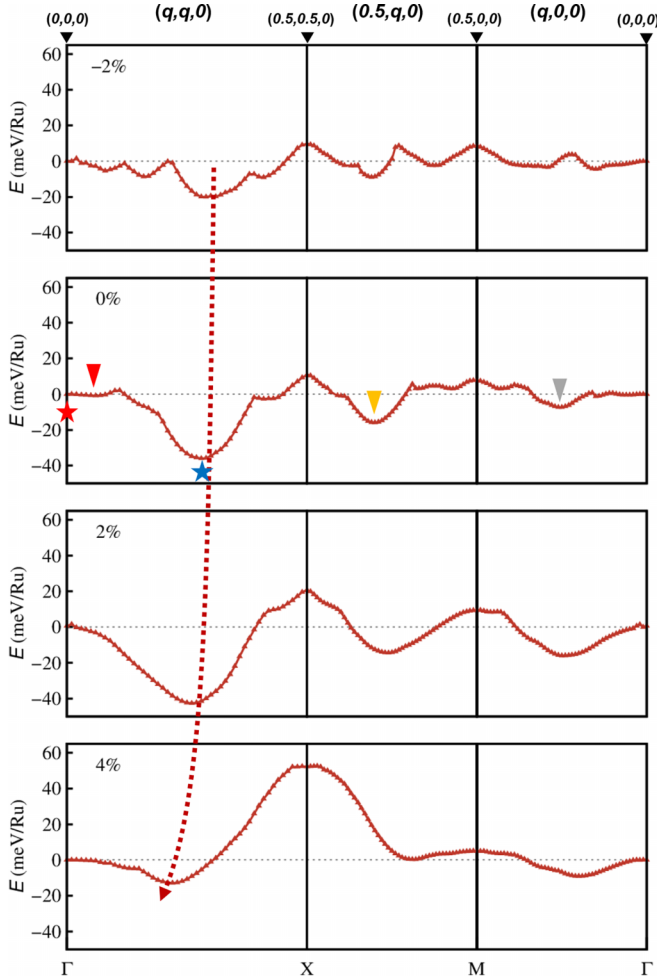


FIG. 1. Energetics of Sr₂RuO₄ upon various spin-spiral \mathbf{q} wave vectors along Γ -X-M- Γ . Here, 0% strain corresponds to the unstrained case, and positive and negative percentages correspond to tensile and compressive strains, respectively. The red and blue stars denote the ferromagnetic and SDW points, respectively, and the red, yellow, and gray ticks denote the local minima for the unstrained case (see text).

discuss for the nonstrained case (0%). We found that the lowest energy is found at $\mathbf{q} = (0.28, 0.28, 0)$ in Γ -X (blue star in Fig. 1), which corresponds to the experimentally observed SDW-type instability \mathbf{q}_{SDW} at $\mathbf{q} \sim (0.3, 0.3, 0)$ [20,21] (From here, we describe the wave vectors in tetragonal reciprocal lattice units, i.e., $\frac{2\pi}{a}$). Our obtained \mathbf{q}_{SDW} position is slightly shifted to the Γ point when compared to the experimental one but gives a reasonable description. As found from the neutron scattering experiment [21], the strongest magnetic instability is located at \mathbf{q}_{SDW} , which corresponds to the Fermi surface nesting vector, and the global minimum from the DFT energetics is located at the same position. The FM fluctuation (red star in Fig. 1), which had been known to be a dominant one, is not in the local minimum position and is energetically much higher (36 meV/Ru) than the one for \mathbf{q}_{SDW} . Interestingly, there is a broad, flat region starting from the Γ point, a FM one, up to $\mathbf{q} \sim (0.1, 0.1, 0)$ in the Γ -X path, which suggests a high density of spin-spiral states and related entropies around the FM instability. This is also observed in the M - Γ path

around Γ . Note that a recent inelastic neutron scattering study reported a broad signal related to the FM fluctuations [27]. This feature is in stark contrast to the sharp peak of the SDW wave vector, which dominates the spin-fluctuation spectrum in the whole Brillouin zone. Our energy calculation closely reproduces the experimental findings. As shown in Fig. 1, the shallow metastability near the Γ point is easily broken by tensile strain, which suggests the fragile nature of the instability due to FM fluctuations. This indirectly explains why no FM order has been found in this compound, while various antiferromagnetic ones (including SDW) have been found with diverse external perturbations [13–17,43].

Aside from the two magnetic fluctuations, SDW and FM, we can identify several instabilities in the energetics curve, denoted by red, yellow, and gray ticks in Fig. 1. First, near Γ , the FM point, the local minimum is found at $\mathbf{q} = (0.06, 0.06, 0)$ within the flat region (red tick in Fig. 1), which is the weakest instability with a very shallow energy well structure among the three metastable ones. It is a continuation of the broad FM fluctuation mentioned before. Susceptibility calculations with the three-band model readily reproduced these FM-like fluctuations. Cobo *et al.* found magnetic fluctuations at $\mathbf{q} = (1/12, 1/12, 0)$ which originated from another interband nesting and are isotropic with respect to the orbitals [30]. Eremin *et al.* also reported the FM-related susceptibility signal at $\mathbf{q} = (0.1, 0, 0)$, which is within the broad region around Γ along the M - Γ path [28]. This magnetic fluctuation is explained as excluding the d -pairing scenario for the superconducting order parameter and promotes p pairing. But, as expected, according to our energetics, this is far weaker than the other types of fluctuations. The $\mathbf{q} = (1/2, 1/4, 0)$ instability (yellow tick in Fig. 1) is the second most dominant feature after the \mathbf{q}_{SDW} one. This is attributed to the intraband nesting from the mostly xy -orbital feature [30,32]. As we will further discuss below, this is also found from our electronic structure calculations. Although not discussed much, this magnetic response was also reported from the previous neutron scattering experiment [21]. A dip along the M - Γ path [$\mathbf{q} = (0.50, 0.30, 0)$], marked with a gray tick in Fig. 1, is related to the nesting grid [21,30,34]. Our thorough energetics calculation clearly demonstrates previous experimental and theoretical instabilities, and the existence of various \mathbf{q} -wave vectors directly shows the complex magnetic structure and instabilities involved in Sr₂RuO₄.

B. Electronic structures for different \mathbf{q} fluctuations

Before delving into the effects of epitaxial strain, it is important to understand how different magnetic fluctuations affect the electronic structure of Sr₂RuO₄. In Fig. 2, we demonstrate the partial density of states (DOS) of the Ru orbitals for the unstrained system. For the nonmagnetic (NM) case, in Fig. 2(a), we can recognize the well-known electronic structure of Sr₂RuO₄: the Van Hove singularity (VHS) peak, which is mainly from the Ru xy orbital, is located slightly above the Fermi level, and the broad two-peak structures from Ru zx/yz orbitals are correctly found. As the Sr₂RuO₄ is close to the Stoner instability, magnetism is expected to relieve the high DOS at the Fermi level and, in this case, also the VHS peak [22]. The effects of the magnetism on the electronic

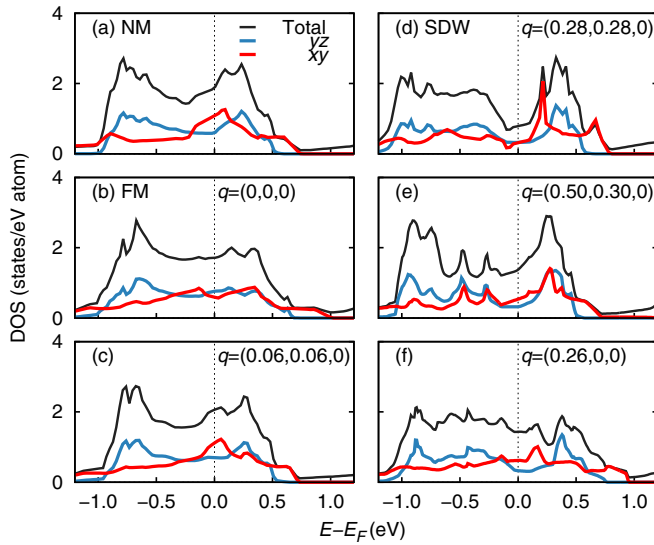


FIG. 2. Total and partial DOSs of unstrained Sr_2RuO_4 for various (meta)stable \mathbf{q} positions: (a) NM, (b) $\mathbf{q} = (0, 0, 0)$ (FM), (c) $\mathbf{q} = (0.06, 0.06, 0)$, (d) $\mathbf{q} = (0.28, 0.28, 0)$ (SDW), (e) $\mathbf{q} = (0.50, 0.30, 0)$, and (f) $\mathbf{q} = (0.26, 0, 0)$. (b)–(d) corresponds to the red star, red tick, blue star, yellow tick, and gray tick in Fig. 1. Here, the total DOS is cut in half ($\times 1/2$).

structures are very different for different \mathbf{q} . In the case of FM, as shown in Fig. 2(b), the VHS from the xy orbital is relieved, and the peaked structure does not remain. Hence, the xy -orbital contribution at the Fermi level is greatly reduced compared to that in the NM case. But ferromagnetism does not significantly alter the structure of the yz/zx orbitals, indicating the FM fluctuation is strongly tied to the xy orbital. While the VHS peak dissipates, the total DOS at the Fermi level is still comparable to that in the NM case, and so is the Stoner instability. For the case of the instability at $\mathbf{q} = (0.06, 0.06, 0)$ [Fig. 2(c)], which is considered to be the continuation of the FM-type fluctuations, the total DOS does not change much from the NM case. The peaked structure of the xy orbital is not relieved in this case, indicating the Stoner instability is not clearly reduced from the FM and near-FM fluctuations. For near-FM fluctuations, there is no orbital-anisotropic behavior like that found from the three-band model [30] [Fig. 2(c)]. This shows that the correlation of ferromagnetism and the xy orbital is very local in \mathbf{q} space, again, indicating the weak role of the FM fluctuation in this system.

For the SDW case [Fig. 2(d)], we can see the strong suppression of the DOS at the Fermi energy with a pseudogaplike feature. Different from the FM case, this strong reduction of DOS at the Fermi level is contributed by all three t_{2g} orbitals and hence is very isotropic. Our findings are in good accord with the previous susceptibility calculation, where the Γ -point fluctuation was mostly from the xy orbital but the SDW one was contributed by all three orbitals [34]. If we assume this SDW-type instability is from the interband nesting of the α and β bands, mostly of yz/zx orbital character, then the orbital-anisotropic behavior is expected. However, the involvement of all three orbitals in the suppression of the DOS shows that the SDW fluctuation is not solely from the nesting physics. In fact, a very recent calculation of uniaxial

strain showed the deviation of the nesting vector from \mathbf{q}_{SDW} [44]. While FM suppresses the VHS from the xy orbitals, SDW shifts the position of the VHS to slightly higher energy without removing the peak itself. This means that the VHS feature is preserved even with the strongest SDW fluctuation. In relation to the reported emergence of the SDW order well beyond the VHS crossing strain [43], our calculations suggest the robustness of the VHS peak with the static magnetic order, which can be an interesting feature and requires further theoretical and experimental investigation.

The instability at $\mathbf{q} = (0.50, 0.30, 0)$ [Fig. 2(e)], indicated as a yellow tick in Fig. 1, is the second dominant fluctuation from the energetics point of view and corresponds to $\mathbf{q} = (1/2, 1/4, 0)$ from previous susceptibility calculations [30,32]. Cobo *et al.* reported the intraband nesting of the xy orbital for this feature [30], and from the partial DOS, there is corresponding suppression of xy orbitals. But we can also observe small changes in the yz/zx ones. Although the suppression is not as obvious as it is for SDW, the clear role of the magnetic fluctuations can still be seen. There is a suggestion that this specific \mathbf{q} plays a leading role in the superconducting order for the uniaxial strained case, and our energetic calculations indicate that this is much more likely than FM fluctuations [32]. The possible merging of this instability with the main \mathbf{q}_{SDW} is suggested, which appears intriguing but requires further confirmation [44]. Another metastable magnetic fluctuation at $\mathbf{q} = (0.26, 0, 0)$ (gray tick in Fig. 1) also shows pronounced effects on DOS, as shown in Fig. 2(f). This seems to be the continuum of nesting-induced SDW [34].

At this point, we want to assert that there is no one-to-one correspondence between the susceptibility calculation and our energetic one. For example, the staggered antiferromagnetic feature at $\mathbf{q} = (0.5, 0.5, 0)$ was reported from the susceptibility calculations, mainly from the xy - xy channel [45,46]. This is not found from our total energetics curve. We think the reason is that all the *other* contributions are naturally included in our DFT calculations and they attenuate the $\mathbf{q} = (0.5, 0.5, 0)$ features. In other orbital channels, the $\mathbf{q} = (0.5, 0.5, 0)$ feature is not quite strong [45]. With the inclusion of the electronic correlation beyond the DFT level, the tendency towards ferromagnetism and antiferromagnetism can be changed, and the details of the energy curve can be modified [34,47]. This might be an intriguing area for additional research. The spin-orbit coupling lifts the degeneracy of the bands and varies the nesting \mathbf{q} vectors by changing the morphology of the Fermi surfaces [48]. While such changes are not very large and our general description remains cogent, the low-energy physics, especially in relation to the superconductivity, is very sensitive to the details of the Fermi surface and can be changed substantially with spin-orbit coupling [45].

C. Role of the epitaxial strain

The epitaxial strain has a significant impact on the overall shape of the energetics curve. Recent intensive studies employing uniaxial strain, which breaks the C_4 symmetry of Sr_2RuO_4 , have provided a unique avenue to understand the superconducting order parameter of the system [43,49,50]. In comparison to the difficult uniaxial approaches, the biaxial

strain, which is typically exercised by epitaxially growing Sr₂RuO₄ on top of substrates such as SrTiO₃, provides a stable route to control the electronic and magnetic properties [51]. The tensile strain moves the \mathbf{q}_{SDW} vector towards the Γ point (see dotted arrow in Fig. 1), which, as we will see below, directly indicates the changes in the Fermi surface nesting feature. Simultaneously, the strain tunes the relative stability of the FM and SDW phases. Starting from -2% , as the system is strained, the SDW phase is further stabilized up to 2% , where the energy difference from the FM one is as high as 43 meV/Ru. Then for the higher strain of 4% , the energy difference between the FM and SDW phases is greatly reduced to 13 meV/Ru. This suggests that through epitaxial engineering, the relative dominance of the SDW phase over the FM phase can be changed and, in turn, can change the spin-fluctuation pairing channels. Given that the external doping stabilizes the magnetically ordered ground states, we can expect the epitaxial strain to play a similar role. Regarding the subdominant $\mathbf{q} = (1/2, 1/4, 0)$ peak, it was previously suggested that if one broke the C_4 symmetry with uniaxial strain, the magnetic order of the same \mathbf{q} would emerge despite the main fluctuation still being the \mathbf{q}_{SDW} one [32]. As $\mathbf{q} = (1/2, 1/4, 0)$ instability is mostly from the xy band or γ sheet, it is expected that the strain, which strongly affects the γ -Fermi surface, can actively tune this specific fluctuations. Rømer *et al.* found that uniaxial strain induces the γ -Fermi sheet crossing the zone boundary through the VHS, which, in turn, enhances this instability [32]. From a previous DFT estimation, C_4 to C_2 symmetry breaking promotes the bifurcation of the next nearest neighbor Ru magnetic exchange interaction, which may promote anisotropic spin fluctuations [35], and there is a possibility of $\mathbf{q} = (1/2, 1/4, 0)$ intraband nesting fluctuations overtaking the SDW interband one. However, for the epitaxial strain in our study, which covers realistic strain ranges, the subdominant $\mathbf{q} = (1/2, 1/4, 0)$ instability, marked with a yellow tick in Fig. 1, cannot overturn the leading \mathbf{q}_{SDW} fluctuations.

Tensile strain smooths the magnetic energy landscape. The local minimum near Γ quickly vanishes, and in the extreme case of 4% strain, the relevant energy scales among local minima become very small, implying that the SDW's dominance is greatly reduced. However, the tendency towards magnetism is enhanced. We discovered that as the tensile strain increases the bond length between Ru sites, the local magnetic moment increases, as expected, and the system becomes more localized. Compared to the complex energetic landscape for the compressive case, the involved magnetism for the 4% strain case is not very complex. In this regime, all the instabilities are very close in energy, and the dominance of nesting-induced SDW fluctuation almost collapses. As we will discuss below, strong tensile strain changes the morphology of the Fermi surface and weakens the nesting feature. The overall energy scales are also reduced for compressive strain. However, this is not due to increased competition among different magnetisms, but rather to the suppression of overall magnetism due to increased itinerancy. The local magnetic moment of Ru at \mathbf{q}_{SDW} is $0.78\mu_B$ for the -2% strain case, which is much smaller than the corresponding value of $1.25\mu_B$ for 4% strain. We found that the compressive strain beyond -2% kills the magnetism of the system even with

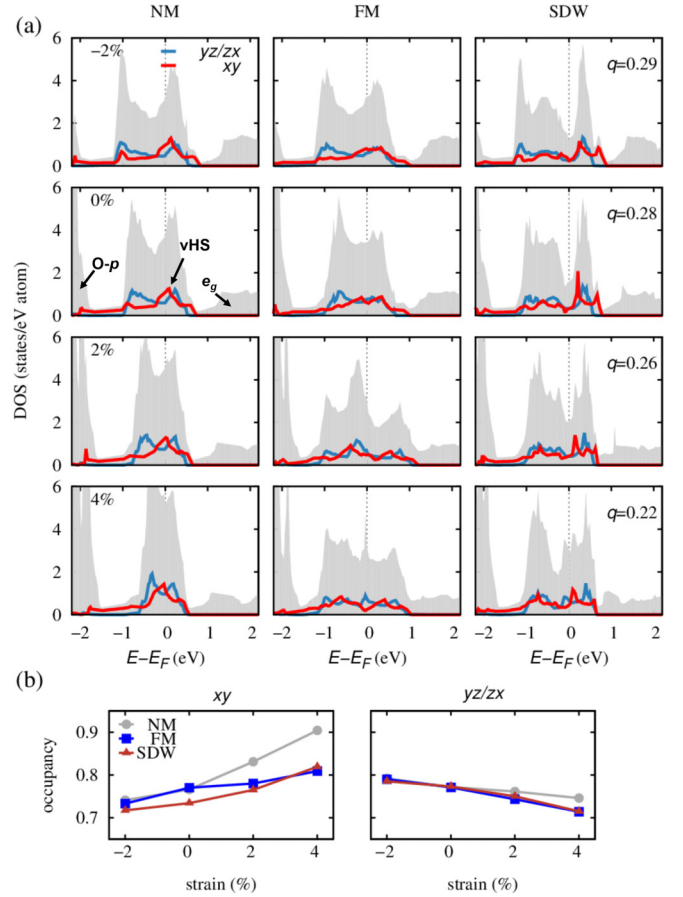


FIG. 3. (a) Total and orbital-resolved partial DOSs of Sr₂RuO₄ for the NM, FM, and SDW cases. For SDW, we plot the case of \mathbf{q}_{SDW} with the minimum energy position for each strain case. Gray denotes the total DOS, red and blue show xy - and yz/zx -orbital-resolved partial DOSs of Ru d . (b) The orbital-resolved occupancy for Ru xy and yz/zx . The occupancy is obtained by integrating the partial DOS of each orbital from -3.0 eV to E_F .

the overestimation tendency of the GGA functionals towards magnetism.

The range of the biaxial strain considered in our study could be accessible thanks to the recent development of the epitaxy technique. Especially for Sr₂RuO₄, demonstrations have already been made [52,53], and employing the membrane technique, we expect even further strain is possible [54].

In Fig. 3(a), we depict the partial DOSs for various strain ranges in the NM, FM, and SDW cases. As the tensile strain is applied, we first see the overall bandwidth of the Ru t_{2g} orbitals is progressively reduced. Especially, the xz/yz orbitals strongly respond to the external strain compared to the xy orbital. Also, upon tensile strain, we can see that the contribution of Ru e_g and O p is progressively enhanced: From the partial DOS in Fig. 3(a), Ru e_g (O p) orbitals move down (up) towards the Fermi energy. The low-energy physics of Sr₂RuO₄ is commonly based on the three-band (t_{2g} orbitals) picture, which can require modifications for the highly tensile strained case due to the involvement of e_g orbitals around the Fermi energy.

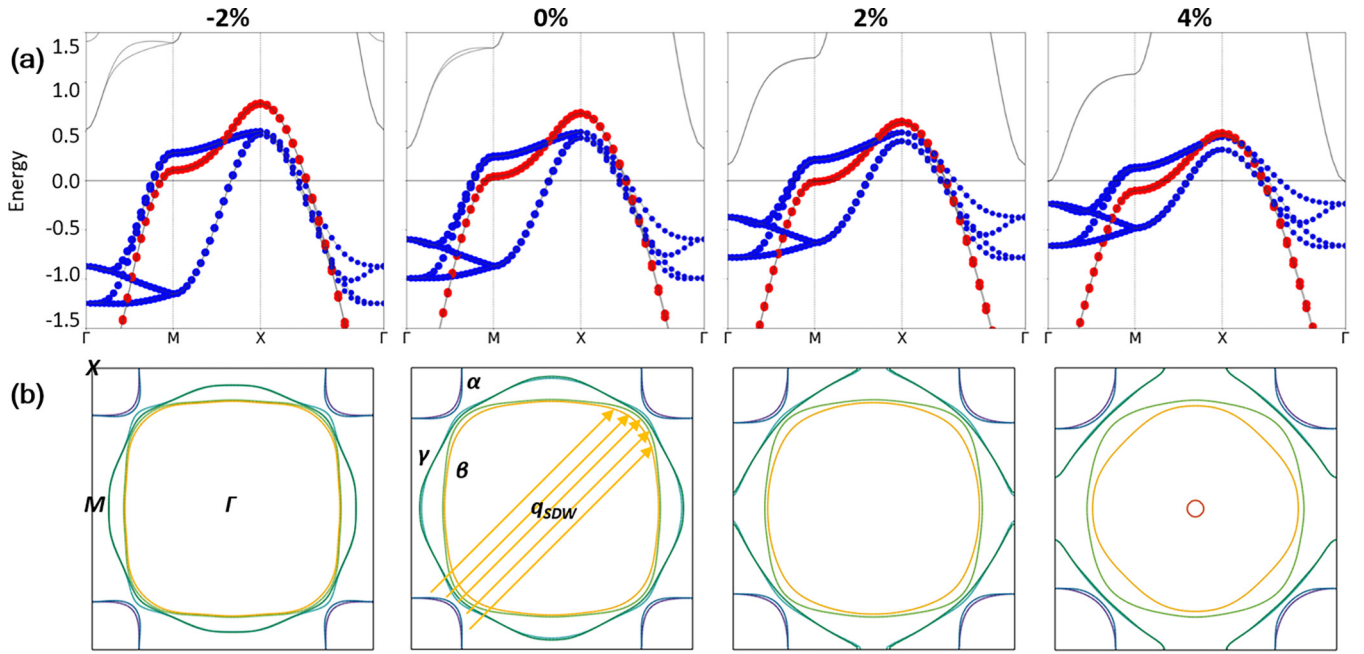


FIG. 4. (a) The band structure and (b) Fermi surface plot for various strain cases in the nonmagnetic phase. For band structure, xy - and yz/zx -projected bands are denoted by red and blue, respectively. Different colors in (b) correspond to different band indices for clarity. In the calculations, a tetragonal unit cell is adopted in which two Ru atoms are included. Therefore, six Ru t_{2g} bands cross the Fermi level in total. The α and β Fermi surfaces are quasi-one-dimensional with yz/zx character, and γ one is two-dimensional with xy character. The arrows in the Fermi surface indicate the \mathbf{q}_{SDW} nesting vector which activates the quasi-1D Fermi surfaces.

From the NM DOS, we see the VHS peak, mostly from the xy orbital, gets even closer to the Fermi energy. Furthermore, the DOS at the Fermi level is greatly increased accordingly, indicating enhanced Stoner instability and, as a result, proximity to the magnetic order. The general electronic structures of the FM and SDW phases do not change much with strain. Interestingly, the VHS peak from the xy orbitals is prominent in the SDW phase as well, and the tensile strain moves the peak towards the Fermi level, as in the NM calculations. This suggests that strain engineering the electronic structure is possible even when the magnetic order sets in Sr_2RuO_4 . As previous studies have shown, the superconducting critical temperature can be increased with epitaxial strain in both the singlet and triplet pictures [52,55,56]. Hence, we believe that direct consideration of magnetic fluctuations in Hubbard-Kanamori-type approaches can offer more insight in this system [35].

Despite the marked differences in the partial DOSs of the FM and SDW cases, the overall orbital-resolved occupancies do not show much distinction. In Fig. 3(b), we display the occupation of each orbital by simply integrating the partial DOS from -3 eV to the Fermi energy. While the value itself has an ambiguity due to the hybridization with O p orbitals, we can clearly observe the expected increasing and decreasing tendency in the occupation of xy and yz/zx orbitals, respectively, as the tensile strain is applied. As shown in Fig. 3(b), due to the tetragonal crystal field, the occupancy of the xy orbitals increases with tensile strain, and yz/zx orbitals show the opposite tendency. Here, we note that the different types of magnetic orders do not have much impact on the occupancy. This may suggest the magnetism itself does not entangle much with the

orbital-dependent electronic behaviors such as orbital-selective Mott phase [57].

D. Fermiology

In Figs. 4(a) and 4(b), we plot the NM band structures and Fermi surfaces for each strain case [58]. Note that the k -dependent spin-spiral electronic structures cannot be described within the generalized Bloch approach. As found from the partial DOS plot, Ru e_g bands progressively shift down and eventually touch the Fermi level at the Γ point in the 4% strain case. We clearly see the bandwidth of xz/yz orbitals is strongly narrowed upon strain, in contrast to the mild change in the xy orbitals [see Fig. 4(a)], as already noted from the DOS in Fig. 3(a). From the Fermi surface, the one-dimensional α pocket enlarges upon the tensile strain, which changes the overall magnitude of the nesting vector and explains the \mathbf{q}_{SDW} movement from X to Γ in Fig. 1. The abrupt change in the \mathbf{q}_{SDW} vector between 2% and 4% tensile strain is further assisted by the γ band. The Lifshitz transition of the γ band is accompanied by the sudden change in the velocity, or the curvature, in the bands [see red band in Fig 4(a)]. The evolution of the Fermi surface as a function of the strain is displayed in Fig. 4(b). The progressive shape change of the γ Fermi sheet from circular to diamond can contribute to the \mathbf{q}_{SDW} nesting, in addition to one-dimensional pockets, and to the electronic susceptibility. However, the morphology of the α and β Fermi surfaces is severely distorted upon tensile strain. Especially, the α pocket is progressively changed from a square to rounded shape. Overall, the nesting effects are weakened and destabilize the SDW, as we see from the energetics landscape in Fig. 1. And we expect the link between

the nesting vector and \mathbf{q}_{SDW} can be progressively severed with the addition of strain. The tensile strain moves the γ pocket edge, which crosses the M point at 2% strain. The shape of the γ sheet changes from a circular to rhombic shape, which indicates enhanced σ bonding over π bonding. For 4% strain, we can see the contribution from the e_g orbitals at Γ . At this limit, the low-energy physics of the system cannot be accounted for with a t_{2g} -only three-band model.

IV. CONCLUSIONS

In conclusion, employing spin-spiral DFT energy calculations, we studied the magnetic energy landscape of Sr₂RuO₄. Besides the SDW and FM fluctuations primarily discussed, we further identified magnetic instabilities, including the $\mathbf{q} = (1/2, 1/4, 0)$ intraband nesting one, which were compared with previous experimental and theoretical findings. By biaxially applying epitaxial strain to the system, we explored the development of magnetic instabilities. We discovered the fragile nature of FM fluctuations and the robust nature of SDW fluctuations. The latter remains the most stable type across all strain levels. Here, we showed that the relative strengths of the instabilities, however, can be tuned upon the addition of external strains. Because tensile strain increases the magnetic propensity of the system, we anticipate that the magnetic order may be established for the very strained case. For compressive strain, the tendency towards magnetism is weakened within

our mean-field calculation, but according to a recent study [44], magnetic fluctuations can be further reduced upon compression, and the possibility of magnetic order should not be abandoned. Recent studies (Refs. [43,44,49], and 50) on symmetry-breaking uniaxial strain can offer key insight to understand the magnetism and superconductivity of the system. On top of these studies, we envisage that biaxial strain can be a functional way to tune the magnetism and, eventually, the superconducting pairing channel of the system in more stable way.

ACKNOWLEDGMENTS

The authors acknowledge the support from the Advanced Study Group program from PCS-IBS. B.K. acknowledges support from NRF Grants No. 2021R1C1C1007017, No. 2021R1A4A1031920, and No. 2022M3H4A1A04074153 and the KISTI Supercomputing Center (Project No. KSC-2021-CRE-0605). M.K. was supported by KIAS Individual Grant No. CG083501. C.-J.K. was supported by NRF Grant No. 2022R1C1C1008200 and the National Supercomputing Center, including technical support from Grant No. KSC-2021-CRE-0580. J.-H.H. acknowledges financial support from the Institute for Basic Science in the Republic of Korea through the Project No. IBS-R024-D1. K.K. acknowledges support from the KAERI Internal R&D Program (Grant No. 524460-22).

-
- [1] Y. Maeno, H. Hashimoto, K. Yoshida, S. Nishizaki, T. Fujita, J. G. Bednorz, and F. Lichtenberg, *Nature (London)* **372**, 532 (1994).
- [2] A. P. Mackenzie and Y. Maeno, *Rev. Mod. Phys.* **75**, 657 (2003).
- [3] Y. Maeno, S. Kittaka, T. Nomura, S. Yonezawa, and K. Ishida, *J. Phys. Soc. Jpn.* **81**, 011009 (2012).
- [4] C. Kallin, *Rep. Prog. Phys.* **75**, 042501 (2012).
- [5] Y. Liu and Z.-Q. Mao, *Phys. C (Amsterdam, Neth.)* **514**, 339 (2015).
- [6] A. P. Mackenzie, T. Scaffidi, C. W. Hicks, and Y. Maeno, *npj Quantum Mater.* **2**, 40 (2017).
- [7] A. Pustogow, Y. Luo, A. Chronister, Y.-S. Su, D. Sokolov, F. Jerzembeck, A. P. Mackenzie, C. W. Hicks, N. Kikugawa, S. Raghu, E. D. Bauer, and S. E. Brown, *Nature (London)* **574**, 72 (2019).
- [8] D. F. Agterberg, *Nat. Phys.* **17**, 169 (2021).
- [9] S. Ghosh, A. Shekhter, F. Jerzembeck, N. Kikugawa, D. A. Sokolov, M. Brando, A. P. Mackenzie, C. W. Hicks, and B. J. Ramshaw, *Nat. Phys.* **17**, 199 (2021).
- [10] S. Benhabib, C. Lupien, I. Paul, L. Berges, M. Dion, M. Nardone, A. Zitouni, Z. Q. Mao, Y. Maeno, A. Georges, L. Taillefer, and C. Proust, *Nat. Phys.* **17**, 194 (2021).
- [11] H. G. Suh, H. Menke, P. M. R. Brydon, C. Timm, A. Ramirez, and D. F. Agterberg, *Phys. Rev. Res.* **2**, 032023(R) (2020).
- [12] S. A. Kivelson, A. C. Yuan, B. Ramshaw, and R. Thomale, *npj Quantum Mater.* **5**, 43 (2020).
- [13] M. Braden, O. Friedt, Y. Sidis, P. Bourges, M. Minakata, and Y. Maeno, *Phys. Rev. Lett.* **88**, 197002 (2002).
- [14] J. P. Carlo, T. Goko, I. M. Gat-Malureanu, P. L. Russo, A. T. Savici, A. A. Aczel, G. J. MacDougall, J. A. Rodriguez, T. J. Williams, G. M. Luke, C. R. Wiebe, Y. Yoshida, S. Nakatsuji, Y. Maeno, T. Taniguchi, and Y. J. Uemura, *Nat. Mater.* **11**, 323 (2012).
- [15] J. E. Ortmann, J. Y. Liu, J. Hu, M. Zhu, J. Peng, M. Matsuda, X. Ke, and Z. Q. Mao, *Sci. Rep.* **3**, 2950 (2013).
- [16] S. Kunkemöller, A. A. Nugroho, Y. Sidis, and M. Braden, *Phys. Rev. B* **89**, 045119 (2014).
- [17] M. Zhu, K. V. Shanavas, Y. Wang, T. Zou, W. F. Sun, W. Tian, V. O. Garlea, A. Podlesnyak, M. Matsuda, M. B. Stone, D. Keavney, Z. Q. Mao, D. J. Singh, and X. Ke, *Phys. Rev. B* **95**, 054413 (2017).
- [18] T. Imai, A. W. Hunt, K. R. Thurber, and F. C. Chou, *Phys. Rev. Lett.* **81**, 3006 (1998).
- [19] Y. Sidis, M. Braden, P. Bourges, B. Hennion, S. NishiZaki, Y. Maeno, and Y. Mori, *Phys. Rev. Lett.* **83**, 3320 (1999).
- [20] M. Braden, Y. Sidis, P. Bourges, P. Pfeuty, J. Kulda, Z. Mao, and Y. Maeno, *Phys. Rev. B* **66**, 064522 (2002).
- [21] K. Iida, M. Kofu, N. Katayama, J. Lee, R. Kajimoto, Y. Inamura, M. Nakamura, M. Arai, Y. Yoshida, M. Fujita, K. Yamada, and S.-H. Lee, *Phys. Rev. B* **84**, 060402(R) (2011).
- [22] I. I. Mazin and D. J. Singh, *Phys. Rev. Lett.* **79**, 733 (1997).
- [23] I. I. Mazin and D. J. Singh, *Phys. Rev. Lett.* **82**, 4324 (1999).
- [24] I. Eremin, D. Manske, S. Ovchinnikov, and J. Annett, *Ann. Phys. (Berlin, Ger.)* **516**, 149 (2004).
- [25] S. Raghu, A. Kapitulnik, and S. A. Kivelson, *Phys. Rev. Lett.* **105**, 136401 (2010).
- [26] M. Tsuchiizu, Y. Yamakawa, S. Onari, Y. Ohno, and H. Kontani, *Phys. Rev. B* **91**, 155103 (2015).
- [27] P. Steffens, Y. Sidis, J. Kulda, Z. Q. Mao, Y. Maeno, I. I. Mazin, and M. Braden, *Phys. Rev. Lett.* **122**, 047004 (2019).

- [28] I. Eremin, D. Manske, C. Joas, and K. H. Bennemann, *Europhys. Lett.* **58**, 871 (2002).
- [29] Q. H. Wang, C. Platt, Y. Yang, C. Honerkamp, F. C. Zhang, W. Hanke, T. M. Rice, and R. Thomale, *Europhys. Lett.* **104**, 17013 (2013).
- [30] S. Cobo, F. Ahn, I. Eremin, and A. Akbari, *Phys. Rev. B* **94**, 224507 (2016).
- [31] Y.-C. Liu, F.-C. Zhang, T. M. Rice, and Q.-H. Wang, *npj Quantum Mater.* **2**, 12 (2017).
- [32] A. T. Rømer, A. Kreisel, M. A. Müller, P. J. Hirschfeld, I. M. Eremin, and B. M. Andersen, *Phys. Rev. B* **102**, 054506 (2020).
- [33] L. Boehnke, P. Werner, and F. Lechermann, *Europhys. Lett.* **122**, 57001 (2018).
- [34] H. U. R. Strand, M. Zingl, N. Wentzell, O. Parcollet, and A. Georges, *Phys. Rev. B* **100**, 125120 (2019).
- [35] B. Kim, S. Khmelevskiy, I. I. Mazin, D. F. Agterberg, and C. Franchini, *npj Quantum Mater.* **2**, 37 (2017).
- [36] G. Kresse and J. Hafner, *Phys. Rev. B* **47**, 558 (1993).
- [37] G. Kresse and J. Furthmüller, *Phys. Rev. B* **54**, 11169 (1996).
- [38] J. P. Perdew, K. Burke, and M. Ernzerhof, *Phys. Rev. Lett.* **77**, 3865 (1996).
- [39] L. M. Sandratskii, *J. Phys.: Condens. Matter* **3**, 8565 (1991).
- [40] J. Kübler, *Theory of Itinerant Electron Magnetism*, International Series of Monographs on Physics (Oxford University Press, Oxford, 2000).
- [41] M. Marsman and J. Hafner, *Phys. Rev. B* **66**, 224409 (2002).
- [42] B. Kim, S. Khmelevskiy, C. Franchini, I. I. Mazin, and K. Kim, *Phys. Rev. B* **101**, 220502(R) (2020).
- [43] V. Grinenko, S. Ghosh, R. Sarkar, J.-C. Orain, A. Nikitin, M. Elender, D. Das, Z. Guguchia, F. Bruckner, M. E. Barber, J. Park, N. Kikugawa, D. A. Sokolov, J. S. Bobowski, T. Miyoshi, Y. Maeno, A. P. Mackenzie, H. Luetkens, C. W. Hicks, and H.-H. Klauss, *Nat. Phys.* **17**, 748 (2021).
- [44] B. Kim, S. Khmelevskiy, C. Franchini, and I. I. Mazin, *Phys. Rev. Lett.* **130**, 026702 (2023).
- [45] O. Gingras, R. Nourafkan, A. M. S. Tremblay, and M. Côté, *Phys. Rev. Lett.* **123**, 217005 (2019).
- [46] O. Gingras, N. Allaglo, R. Nourafkan, M. Côté, and A.-M. S. Tremblay, *Phys. Rev. B* **106**, 064513 (2022).
- [47] M. Kim, C.-J. Kang, J.-H. Han, K. Kim, and B. Kim, *Phys. Rev. B* **106**, L201103 (2022).
- [48] A. Tamai, M. Zingl, E. Rozbicki, E. Cappelli, S. Riccò, A. de la Torre, S. McKeown Walker, F. Y. Bruno, P. D. C. King, W. Meevasana, M. Shi, M. Radović, N. C. Plumb, A. S. Gibbs, A. P. Mackenzie, C. Berthod, H. U. R. Strand, M. Kim, A. Georges, and F. Baumberger, *Phys. Rev. X* **9**, 021048 (2019).
- [49] C. W. Hicks, D. O. Brodsky, E. A. Yelland, A. S. Gibbs, J. A. N. Bruin, M. E. Barber, S. D. Edkins, K. Nishimura, S. Yonezawa, Y. Maeno, and A. P. Mackenzie, *Science* **344**, 283 (2014).
- [50] A. Steppke, L. Zhao, M. E. Barber, T. Scaffidi, F. Jerzembeck, H. Rosner, A. S. Gibbs, Y. Maeno, S. H. Simon, A. P. Mackenzie, and C. W. Hicks, *Science* **355**, eaaf9398 (2017).
- [51] M. E. Barber, A. Steppke, A. P. Mackenzie, and C. W. Hicks, *Rev. Sci. Instrum.* **90**, 023904 (2019).
- [52] B. Burganov, C. Adamo, A. Mulder, M. Uchida, P. D. C. King, J. W. Harter, D. E. Shai, A. S. Gibbs, A. P. Mackenzie, R. Uecker, M. Bruetzam, M. R. Beasley, C. J. Fennie, D. G. Schlom, and K. M. Shen, *Phys. Rev. Lett.* **116**, 197003 (2016).
- [53] J. P. Ruf, H. Paik, N. J. Schreiber, H. P. Nair, L. Miao, J. K. Kawasaki, J. N. Nelson, B. D. Faeth, Y. Lee, B. H. Goodge, B. Pamuk, C. J. Fennie, L. F. Kourkoutis, D. G. Schlom, and K. M. Shen, *Nat. Commun.* **12**, 59 (2021).
- [54] S. S. Hong, M. Gu, M. Verma, V. Harbola, B. Y. Wang, D. Lu, A. Vailionis, Y. Hikita, R. Pentcheva, J. M. Rondinelli, and H. Y. Hwang, *Science* **368**, 71 (2020).
- [55] Y.-T. Hsu, W. Cho, A. F. Rebola, B. Burganov, C. Adamo, K. M. Shen, D. G. Schlom, C. J. Fennie, and E.-A. Kim, *Phys. Rev. B* **94**, 045118 (2016).
- [56] Y.-C. Liu, W.-S. Wang, F.-C. Zhang, and Q.-H. Wang, *Phys. Rev. B* **97**, 224522 (2018).
- [57] A. Koga, N. Kawakami, T. M. Rice, and M. Sigrist, *Phys. Rev. Lett.* **92**, 216402 (2004).
- [58] A. M. Ganose, A. Searle, A. Jain, and S. M. Griffin, *J. Open Source Software* **6**, 3089 (2021).